Journal of Sound and Vibration (1998) **218**(2), 177–204
Article No. sv981681

HIGH FREQUENCY NOISE GENERATION IN SMALL AXIAL FLOW FANS

D. A. QUINLAN

Acoustics Research Department, Bell Laboratories, Lucent Technologies Inc.,
600 *Mountain Ave., Murray Hill, NJ* 07974, *U.S.A.*

AND

P. H. BENT

Boeing Commercial Airplane Group, P.O. Box 3707, *Mail Stop* 67-*ML, Seattle,*
WA 98124-2207, *U.S.A.*

(*Received* 9 *September* 1996, *and in final form* 14 *January* 1998)

This paper presents results from an investigation of the broadband sources of acoustic noise in small axial flow fans. Observations drawn from flow visualization experiments and fluid dynamic measurements indicate that secondary flows are primary contributors to the broadband noise generated by small axial flow fans. More specifically, flow unsteadiness associated with tip gap flows is identified as a primary source of high frequency noise. As air is forced through the tip gap (i.e. the space between the rotating blade tip and the stationary housing), the flow rolls up forming vortices at the blade tip. These vortices convect into the blade passage and become the dominant source of unsteadiness in the blade passage and at the fan exit plane. The data presented indicates that this turbulence is the dominant source of noise above 1·5 kHz for the fan tested. The likely radiation mechanisms are trailing edge scattering, and radiation from free turbulence and/or boundary layers. Three types of experiments were performed as part of the study. First, flow visualization tests were run in an attempt to obtain a subjective evaluation of the flowfield. Then, stationary and rotating hot-wires were used to provide mean velocity and turbulence intensity data for non-radial flow components. Using the results from the flow visualization and hot-wire tests, possible noise generation mechanisms were postulated. Fan modifications were then made to test the viability of the proposed noise contributors. The addition of flanges to the blade tips and of fabric near the blade trailing edges provided up to a 9 dB decrease in sound power above 1 kHz. These results will need to be coupled to an analogous study of low frequency noise generation (i.e. below 1 kHz) for a significant reduction in perceived noise level to be achieved.

1. INTRODUCTION

A dominant trend in the physical design of electronic systems is the continuing rise in system heat dissipation. For example, the typical heat dissipation value in large telecommunication switching frames has increased by an order of magnitude over the past 5 years. The trend is being driven by a rapid rise in circuit densities and a push toward much smaller system footprints. One of the penalties of this

0022–460X/98/470177 + 28 $30.00/0

trend is an associated increase in radiated acoustic noise. Since these systems are cooled wih air-moving devices, the increase in dissipation demand results in higher fan speeds and an increase in the number of installed fans [1].

While conventional noise control methods such as fan speed control have proven to be effective in reducing cooling fan noise, these solutions are inherently limited by the minimum noise that a given fan design will produce [2]. Further progress in small air-moving device noise control has been limited by the lack of detailed information regarding underlying aeroacoustic processes. This is particularly true for broadband noise which has not been studied to the degree that tonal noise generation has been examined [3, 4]. One avenue for reducing noise may be the use of active noise control. In fact, studies have shown active control to be an effective method for the reduction of low frequency blade tones [5–7]. However, the full potential of active control can not yet be conclusively assessed because all of the pertinent aeroacoustic processes have not yet been identified. Unless a thorough understanding of the underlying physics exists, the application of active control schemes to noise problems usually proves to be fruitless.

Whether an active or passive approach is taken, it is clear that to advance the state-of-the-art further detailed identification of all the primary aeroacoustic processes in small axial flow fans is needed. The intent of the work described here was to address this problem by initiating an investigation of key source mechanism(s). Based upon the assumption that different processes dominate particular frequency bands, the specific goals of the work described here revolved primarily around high frequency noise.

There were three main components to the study. The first involved the application of flow visualization techniques. The flow visualization provided a subjective view of the general properties of the flowfield. The second component was to make fluid dynamic measurements in the flowfield in order to quantify local mean velocities and turbulence intensity values. Finally, the last component involved simple acoustic comparison tests. An additional component (discussed in reference [8]) was the experimental investigation of the dependence of sound power upon characteristic flow velocity.

2. EXPERIMENTAL FACILITIES

2.1. ANECHOIC WIND TUNNEL

In order to provide controlled flow conditions and to provide suitable conditions for acoustic measurements, many of the measurements described here were performed in an anechoic wind tunnel (see Figures 1 and 2). The wind tunnel consisted of a bellmouth inlet followed by a duct contraction which was used as a venturi volume flow rate meter. Located at the inlet was a grid that supported dense gauze screens. The screens covered the entire inlet and were used to control the tunnel flow rate. An anechoic termination was located just downstream of the duct contraction. This termination was used to minimize acoustic standing waves in the facility. The next component was a constant diameter (15 cm i.d.) test section which contained the test fan. Downstream of the fan was a second anechoic

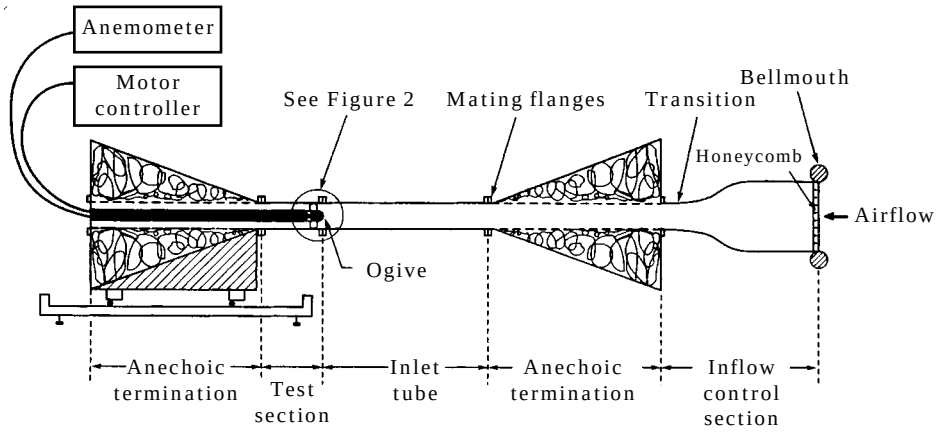

Figure 1. Schematic diagram of anechoic wind tunnel test facility. (Sketch not drawn to scale.)

termination. A variable speed motor used to drive the fan was mounted in a 7·6 cm dia. tube which ran along the center of the duct, on the downstream side of the fan. Motor, shaft encoder and sensor cabling was located within this inner tube.

The operating point of the fan was monitored by measuring the flow velocity and fan pressure rise. One set of circumferential pressure taps was located upstream of the duct contraction, and a second set was located downstream of the duct contraction (4 taps per location). Each set provided an average pressure for the relevant location. The contraction pressure difference was measured using an MKS Baratron 220CD pressure transducer. The flow rate was calculated using the pressure measurements and Bernoulli's equation. Similarly, the fan pressure rise was measured using two sets of circumferential pressure taps located near the fan inlet and outlet (again, 4 taps per location). This pressure difference was also measured using an MKS Baratron 220CD transducer. In order to overcome losses within the facility, a booster fan was attached to the outlet termination when high

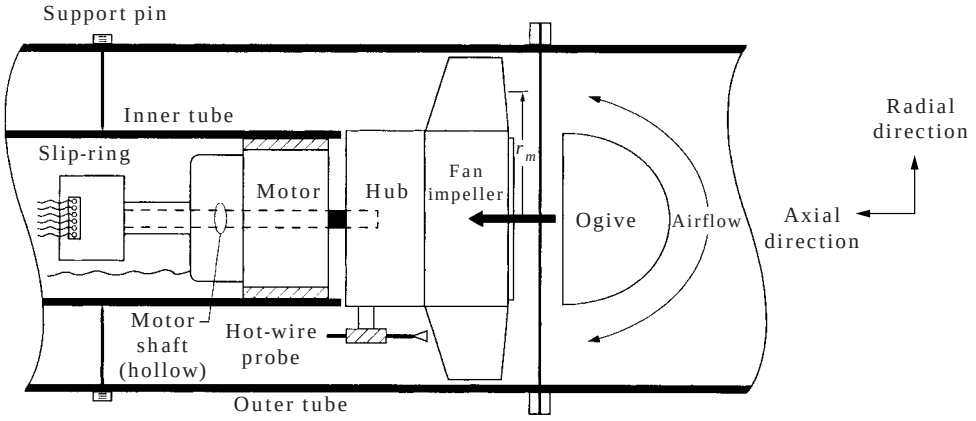

Figure 2. Schematic diagram of test section from wind tunnel test facility. The test fan blade shape was significantly more complicated than depicted here. Various custom hot-wire probes and supports were used to make measurements within the blades passages. (Sketch not drawn to scale.)

flow rate fan performance measurements were made (see section 2.3). The booster fan was an EBM W4S300 driven through an isolation transformer by a Ramsa 9220 amplifier and a Tektronix CFG280 function signal generator. (Note: the wind tunnel booster fan was required only for operation above a non-dimensional flow rate equal to 0·4.)

As shown in Figure 2, the fan mounting hub was designed to accommodate a hot-wire probe holder so that fluid dynamic measurements could be made within the rotating impeller. Stationary hot-wire measurements were also performed by inserting hot-wires through access ports in the outer tube. These ports were located upstream and downstream of the impeller.

Phase-averaged velocity data and exit plane velocity spectra were acquired using a Concurrent 6300 data acquisition computer. This data was low-pass filtered in accordance with the Nyquist criterion using Stanford Instruments SR-650 filters. The rotating wire and the acoustic data were acquired using a PC-based National Instruments data acquisition card with sigma-delta converters.

2.2. AIR-MOVING DEVICE TEST PLENUM

A second facility used as part of this study was the ANSI S12.11 fan test plenum shown in Figure 3 [9]. The fan test plenum was designed to approximate typical installation conditions while providing a means for consistent measurement of air-moving device noise emission as a function of operating point. Mylar was selected as the plenum covering since it is air-tight and has a very low acoustic transmission loss over the typical frequency range of interest. The fan mounting area consisted of an aluminum plate fixed in the center of a large rubber membrane. Fans were attached to the plenum via an attachment plate. An

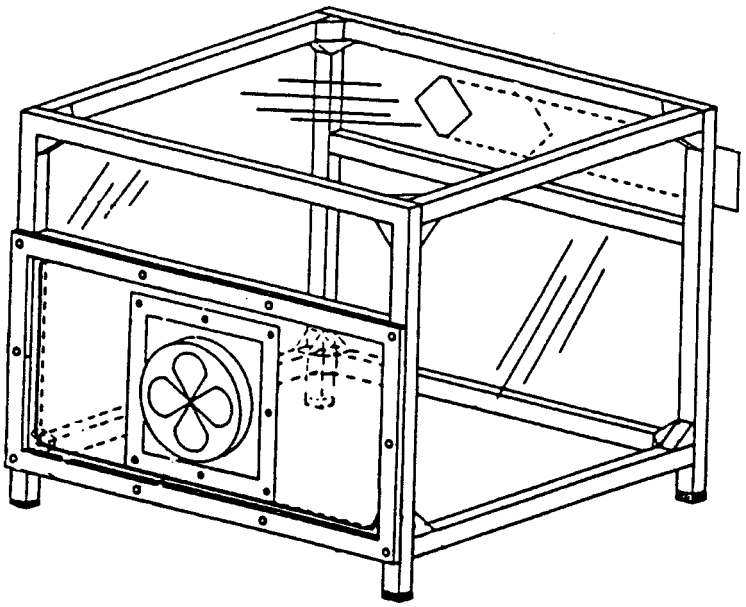

Figure 3. Sketch of ANSI S12.11 air-moving device test plenum. (Not drawn to scale.)

TABLE 1

Dimensions of test fan

	Hub	Tip
Radius (cm)	3·8	7·1
Chord length (cm)	5·2	5·2
Inlet angle	20°	13°
Discharge angle	55°	30°

aluminum slider was used to change the static pressure in the plenum (i.e. alter the aerodynamic load). A piezometric ring mounted within the frame was used to monitor the internal static pressure. The plenum pressure was measured using a MKS Baratron 220CD pressure transducer.

Given the outlet area of the opening and the static pressure within the box, the fan operating point was monitored using the method described by Taylor [10].

2.3. TEST FAN DESCRIPTION AND PERFORMANCE CURVES

The fan examined in this study was a Papst Model 6248. The 6248 was selected because its design is representative of the small axial fans used in electronic systems where high reliability is required. The specific design details of this 5-bladed fan are given in Table 1.

The measured non-dimensional performance curves for the test fan are shown in Figure 4. The non-dimensionalized pressure rise, ψ, and flow rate, ϕ, are defined as follows:

$$\psi = \frac{\Delta p}{\rho V_{tip}^2}, \qquad \phi = \frac{Q}{A_{fan} V_{tip}}, \tag{1, 2}$$

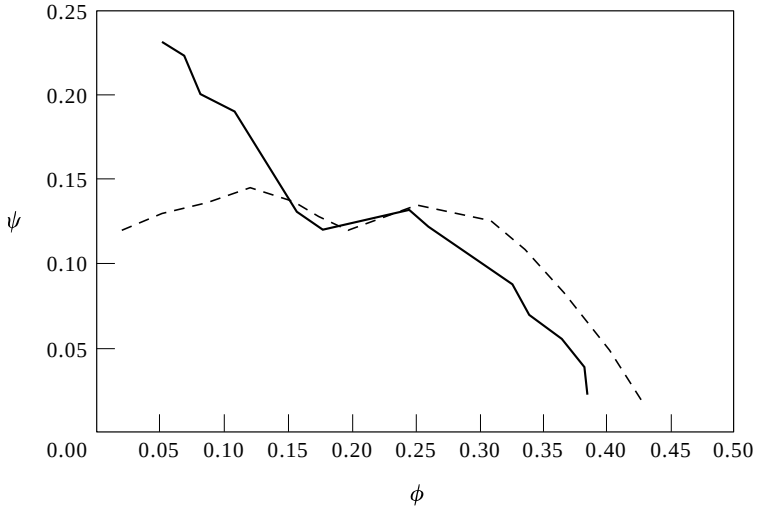

Figure 4. Fan performance curves as measured in anechoic wind tunnel (——) and ANSI S12.11 test plenum (——). Over the performance range of interest ($0{\cdot}25 < \phi < 0{\cdot}35$), the maximum measurement error was 4%.

where Δp is the static pressure rise across the fan, ρ is the density of air, V_{tip} is the fan tip speed, Q is the volumetric flow rate, and A_{fan} is the exit area of the fan (defined as $[\pi(r_{tip}^2 - r_{hub}^2)]$). As Figure 4 shows, the plenum performance curve had the characteristic shape associated with small axial fans, with the useful operating range beginning at approximately $\phi = 0{\cdot}25$. The curve measured in the wind tunnel was found to be significantly different from the plenum curve but the cause of the differences was not determined. Some possible causes are discussed below. In electronic systems, fans typically operate at flow rates above best efficiency (including a design margin that prevents possible unstable performance) and below free delivery. As such, the performance region of interest in this study was $0{\cdot}25 < \phi < 0{\cdot}35$. The two performance curves were shown to be repeatable with a maximum measurement error of 4% over this performance range.

When considering the differences in the two performance curves, there are four factors to consider. First, the outflow conditions were significantly different in the two facilities. Thus, the static pressure recovery was quite different in the two facilities, particularly at low flow rates. Second, the inlet boundary layers would be expected to be very different in the two facilities given the differences in inlet conditions. Third, the blade design appeared to be optimized for axial inflow at all radial locations, and such inflow conditions could only be achieved when the fan was operating in the wind tunnel above the best efficiency point ($\phi \approx 0{\cdot}25$). Finally, the accuracy of the measurements themselves may also have contributed to the differences, particularly at low flow rates.

3. FLOW VISUALIZATION

In order to gain a qualitative understanding of the flow-field developed within and around the impeller passages, two types of flow visualization experiments were performed. The experiments were run in both of the facilities described above. Over the performance range of $0{\cdot}25 < \phi < 0{\cdot}35$, the general results described below were similar for both facilities.

3.1. ACENEPHTHENE CRYSTALS

In the first set of experiments, a solution containing acenephthene crystals was air brushed onto the blades of a test impeller. This process left a white residue on the blade surface. In the presence of flows with high shear stress (e.g. turbulent flows, leading edge boundary layers, etc.), the acenephthene was sublimated to a gaseous state and was removed from the blade surface leaving the normal black surface of the blade exposed [11]. When applied judiciously, this technique could be used to identify regions of the blades which were subjected to turbulent flows.

Acenephthene-coated impellers were run at a variety of speeds and operating points. In general, the results did not indicate the presence of any obvious disturbances (such as flow separation regions) that could be easily linked to potential noise generation mechanisms. The areas where the coating was consistently sublimated were on the suction side of the blades, near the blade

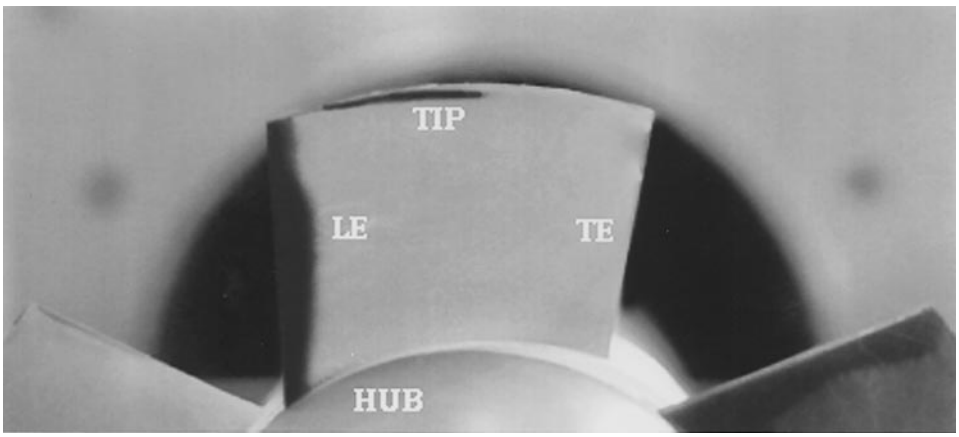

Figure 5. Photograph showing erosion points on acenephthene-coated blade after operation in anechoic wind tunnel and with non-dimensional flow rate set $\phi = 0{\cdot}3$. View is of low pressure (i.e. suction) side of blades. Impeller was rotating counter-clockwise during the test. Similar results were observed when impeller was run using the ANSI plenum.

leading edges and the blade tips. These features can be seen in Figure 5 which contains a photograph of the suction side of a test impeller that was operated at $\phi \approx 0{\cdot}3$. The erosion of the acenephthene at the blade leading edges was likely due to the laminar boundary layer which would be thin at this location. However, the cause of the narrow erosion path along the blade tips was not immediately recognized.

3.2. SMOKE FLOW VISUALIZATION

In the second set of experiments, smoke was drawn into the flowfield at the inlet of the test fan and the resulting movement of the smoke was observed. Initially, the smoke was ingested into the passage from unpressurized acetic acid smoke tubes placed at various upstream locations. For the case of the plenum tests, these positions included locations next to the housing and out of the direct inflow. A strobe light triggered by an optical shaft encoder was used to "freeze" the motion of the impeller and to allow the movement of the smoke to be observed. (When these tests were run in the wind tunnel, the test section outer tube shown in Figure 2 was made of plexiglass.) In order to concentrate the smoke so that the disturbances could be photographed, a 1 mm dia. Pitot tube was attached to an acetic acid smoke tube and this combination was used as a smoke generating probe. The smoke was forced through the probe using compressed air. By moving the narrow diameter jet of white smoke to locations upstream of the fan, flow patterns in-and-around the blades could be photographed.

At operating points below best efficiency point, the flow in the blade channels was highly turbulent. This was caused by recirculation of the flow from the outlet of the fan to the inlet. As the operating point was moved above the best efficiency point of the fan, the turbulence due to recirculation was no longer observed, as would be expected. However, the flow in the blade channels was still somewhat turbulent toward the back of the blade passages (i.e. in the vicinity of the trailing

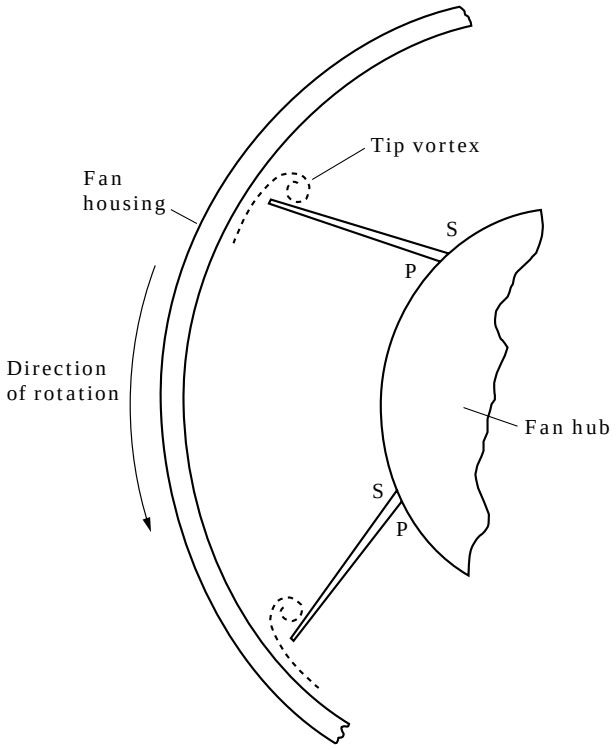

Figure 6. Sketch of tip vortex formation in a turbo machine. (This figure is not drawn to scale and is not intended to fully depict blade geometry.)

edges of the blades). Further experimentation demonstrated that this turbulence was associated with vortices formed at the blade tips.

As shown in Figure 6, tip vortices are formed when flow through the tip gap flow "rolls up" after it passes out of the tip gap onto the suction side of the blade. The tip gap flow is caused by the pressure differential present between the pressure and suction sides of the rotating blade. As shown in the drawing, the tip gap flow is not axial and, as such, does not provide a positive contribution to the work being done by the fan. It is well-known that these tip gap flows can be a source of aerodynamic inefficiency and acoustic noise in fans (see, for example, references [11–14]). However, the details (i.e. radiation mechanisms, relevant frequency bands, flowfield velocity contours, etc.) have not been studied completely, especially for the case of small axial flow fans.

Figure 7 contains a typical video image of smoke flow in a section of a blade passage. The tip vortex is the conical structure near the centre of the photograph. The tip vortex was observed to originate near the leading edge (LE) of the blades, at a location approximately 3/4 of the distance from the trailing edge (TE) to the LE. This was the point of maximum blade thickness and would normally also be the location of maximum blade lift. At this location, the diameter of the tip vortex was small, on the order of 1 mm. Going from this location downstream towards the TE, the vortex diameter increased until, at roughly 1/2 to 2/3 of the distance

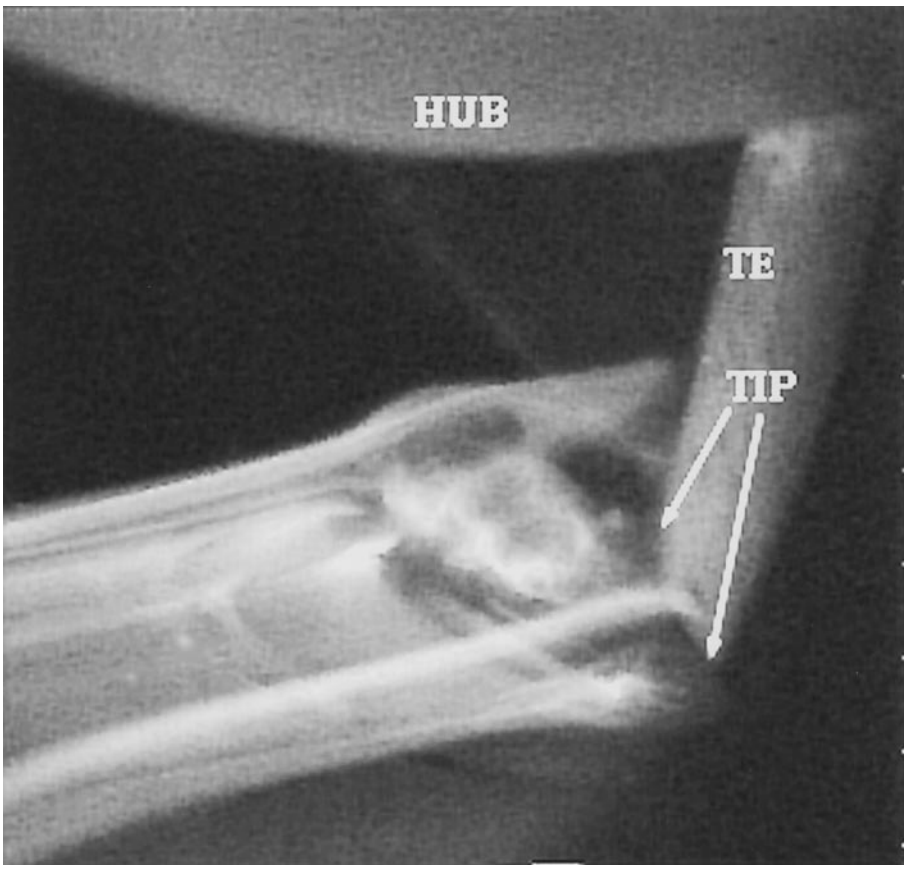

Figure 7. Photograph of tip vortex formation in the test fan. Impeller is rotating counter-clockwise. Partial view of one blade is seen on right side. (View of leading edge is obstructed by housing—lower right hand corner of figure.) Note that vortex has lifted off the blade near the location of the rear arrow.

from TE to LE, the vortex "lifted off" of the blade surface. (The point and angle at which the vortex lifted off varied with operating point. The general trend was such that it tended to lift off nearer the trailing edge and at a shallower angle with respect to the blade as the fan loading was reduced.) The rear arrow in Figure 7 indicates the approximate position where the vortex lifted off for this particular test.

Presumably, it was this vortical disturbance which caused the erosion of the acenephthene coating along the tip that was described in the previous section. Comparing the photographs in Figures 5 and 7, the sublimation area along the tip corresponds to the formation region of the tip vortex flow. The smoke visualization demonstrated that the erosion was not observed on the tip near the TE because the vortex had lifted off the blade surface before that point.

The smoke visualization further demonstrated that, after leaving the blade surface, the vortex convected downstream into the rear of the blade passage. As the vortex convected away, the diameter of the largest eddies became comparable

to 1/2 to 3/4 of the blade span. Near the fan exit, the vortical disturbance broke-up into a more chaotic disturbance. As will be demonstrated in subsequent sections, this turbulent flow contributed significantly to flow unsteadiness near the following blade, near the trailing edge.

4. FLUID DYNAMIC MEASUREMENTS

4.1. OVERVIEW OF WIND TUNNEL MEASUREMENTS

In order to obtain a more detailed insight into the impeller flowfield, a series of fluid dynamic measurements were performed using the wind tunnel facility. Measurements were made at a variety of locations in and around the fan impeller. The measurements were made using hot-wire sensors mounted in both rotating-frame (i.e. rotating with the impeller) and fixed-frame locations.

As is typically done, the instantaneous velocity signal, $v(\theta, r, x, t)$, has been decomposed here into the sum of a phase averaged mean component, $V(\theta, r, x)$, and an instantaneous variation from this mean, $\dot{v}(\theta, r, x, t)$, i.e.

$$v(\theta, r, x, t) = V(\theta, r, x) + \dot{v}(\theta, r, x, t). \tag{3}$$

For a fixed radial and axial position, the normalized mean flow velocity, $V_m(\theta)$, and phase averaged turbulence intensity, $V_t(\theta)$, can then be expressed as

$$V_m(\theta) = \frac{mean[v(t, \theta)]}{V_{tip}}, \qquad V_t(\theta) = \frac{\dot{v}(\theta)_{rms}}{V_{tip}} = \frac{\left(\frac{1}{n}\sum_{i=1}^{n}[v_i(t, \theta) - V_m(\theta)]^2\right)^{1/2}}{V_{tip}}, \tag{4, 5}$$

where n is the number of averages used. The fan tip speed scaling was used because it provided a normalization that was independent of the local velocity, and therefore, allowed direct comparison of data taken at different measurement locations and rotational speeds.

The fixed-frame measurements were performed using TSI 1210-T1.5 sub-miniature tungsten hot-wire sensors and a TSI IFA-100 anemometer. The rotating frame measurements were performed using custom-designed TSI sensors similar to the 1210-T1.5 sensors. Calibration measurements were made with a TSI Model 1125 calibrator. Fourth-order polynomial fits to the calibration data were computed and the resulting calibration coefficients were down-loaded into the data acquisition program. The voltage-to-velocity conversion was performed during the data acquisition.

The goal of the hot-wire measurements was to determine the general properties of the flowfield. The intent was not to fully resolve flow vectors but to get an indication of magnitude. Full resolution of all flow components would have required the use of a more complex sensor arrangement. In each measurement, the hot-wire sensor was mounted such that it had maximum sensitivity in the axial

and tangential flow directions, and minimum sensitivity in the radial flow direction. For the case of the rotating sensor measurements, this sensor orientation was assumed to provide a good indication of the overall magnitude of flow velocity since the radial flow components would be relatively weak (in general) within the blade passages.

4.2. STATIONARY SENSOR MEASUREMENTS

In the stationary-frame measurements, the hot-wire sensor was mounted 1·5 mm downstream of the fan impeller. Measurements were made at radial locations corresponding to the blade root, mid-span and tip.

The hot-wire voltage signal was acquired simultaneously with the output of the optical shaft encoder. The encoder signal was used as a marker in the time record, providing a means for ascertaining the angular position of the impeller as a function of time. The data was synchronously averaged to provide average values of $V_m(\theta)$ and $V_t(\theta)$ as a function of angular position. For the data presented here, the number of averages (n) was 100.

Figure 8 shows the phase averaged turbulence intensity ($V_t(\theta)$) measured at the mid-span location (i.e. halfway between the root and tip of the blade). In this plot, the data shown is an averaged result taken over the five blade passages. Note that the location of the trailing edge is marked as TE, and that the suction and pressure sides of the blades are identified using S and P, respectively. The ensemble-averaged time series for $0{\cdot}20 \geqslant \phi \geqslant 0{\cdot}35$ are shown. The peaks in the plots do not occur at the exact TE position because the sensor was 1·5 mm downstream of the blade. Consequently, there was a time lag corresponding to the time required for the wake to convect past the sensor.

Beginning at $\phi = 0{\cdot}20$, the turbulence intensity was relatively flat across the passage with the levels being between 0·08 and 0·13. At this operating point, the flow would be expected to be quite turbulent since the loading is high and flow was recirculating through the passages. As the loading decreased and the value of ϕ approached 0·35, the turbulence intensity in the region between the blades decreased to as low as 0·01.

The key feature to note is that the turbulence intensity values tended to be higher near the pressure side of the blades, as compared to the suction side of the blades. This tends to support the observation discussed in section 3.2, that the tip vortices seemed to be bursting in the blade passages and that related flow unsteadiness contributed significantly to the turbulence present at the trailing edges of the blades. The turbulence intensity values tended to be low near the suction sides of the blades, again indicating that any flow separation over the blade was relatively weak.

Figure 9 contains an analogous set of plots for a sensor placed 1·5 mm downstream of the blade at the tip radial location. Generally, the tip turbulence intensity values are higher than those seen at the mid-span. This feature is especially noticeable at high ϕ values in the region between the blades. For example, for $\phi = 0{\cdot}35$, the turbulence intensity is an order of magnitude higher in amplitude in this region as compared to the mid-span data. This may be due to a build-up of a turbulent boundary layer along the facility wall.

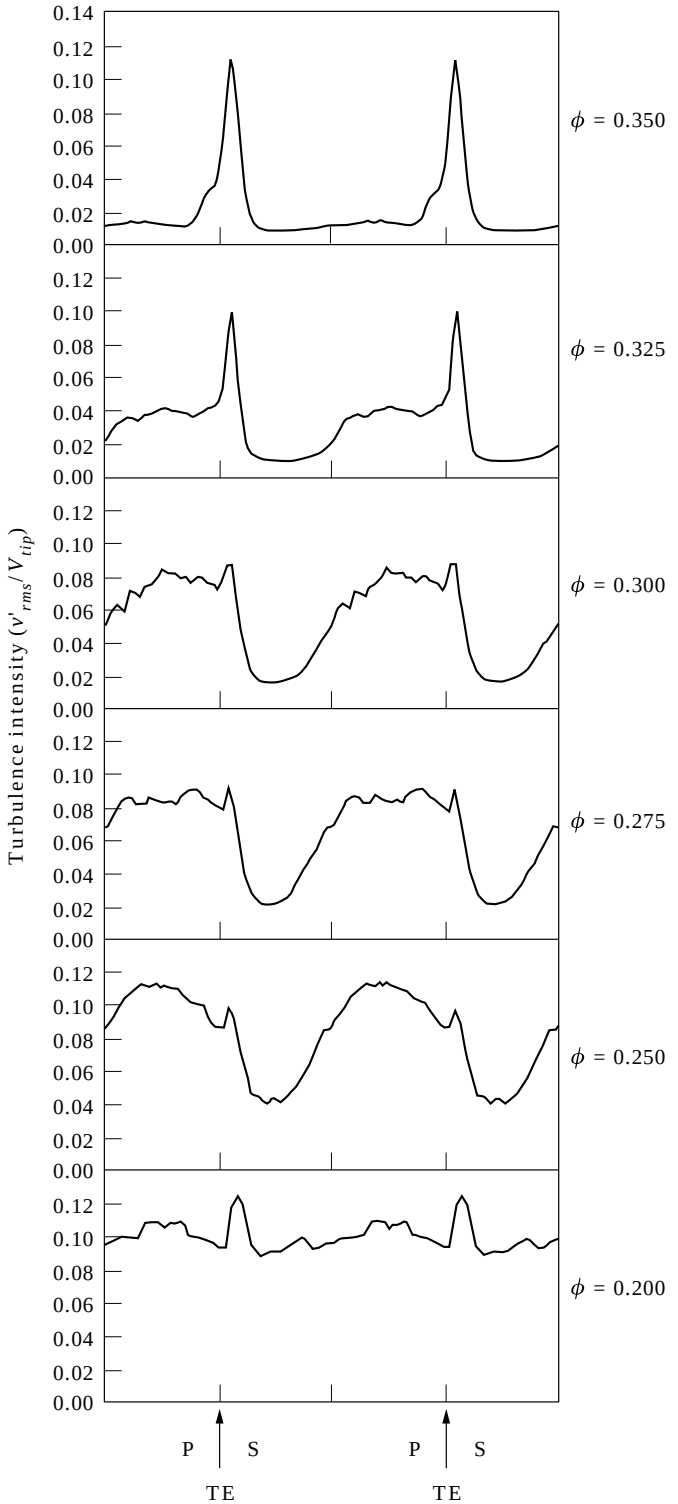

Figure 8. Phase-averaged turbulence intensity measured at the blade mid-span for $0{\cdot}2 \leqslant \phi \leqslant 0{\cdot}35$. Data taken using stationary hot-wire located 1·5 mm downstream of blade trailing edge. P and S are the high and low pressure sides of the blades, respectively.

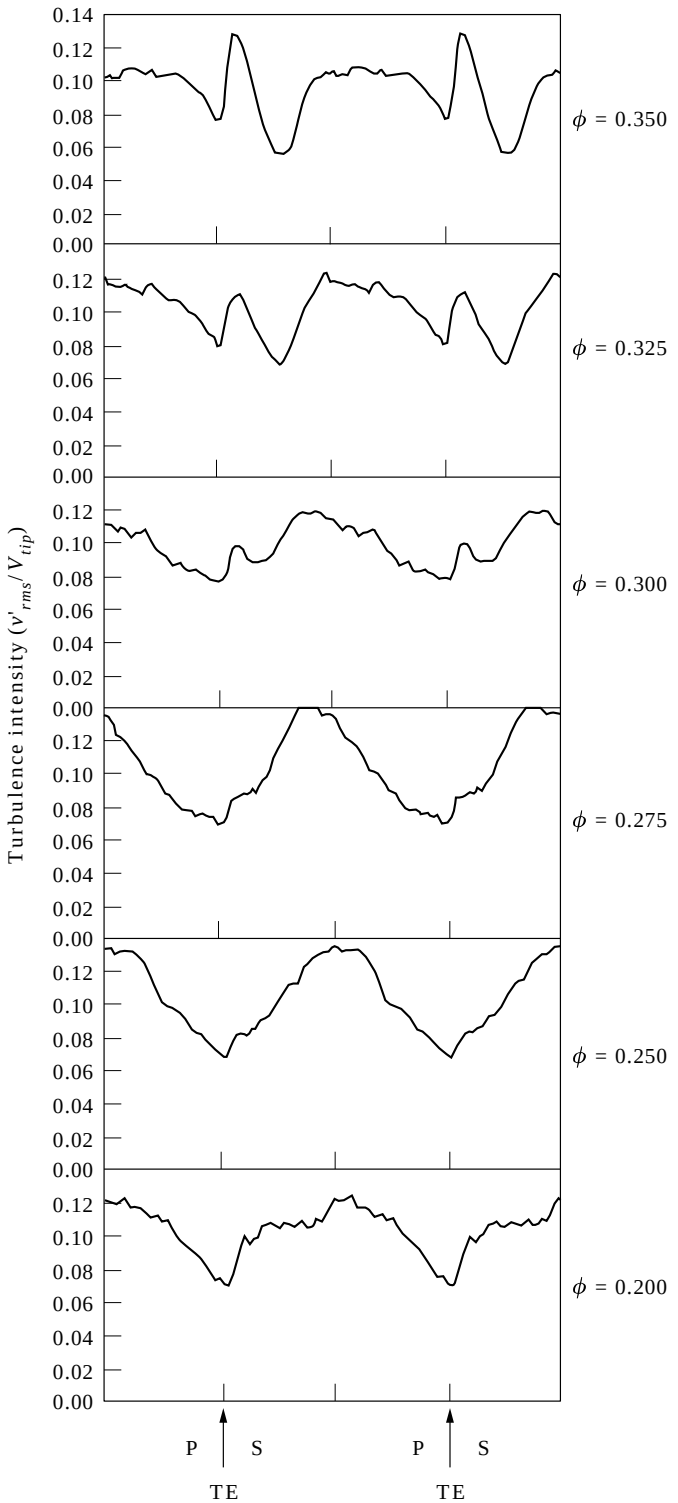

Figure 9. Phase-averaged turbulence intensity measured at the blade tip for $0{\cdot}2 \leqslant \phi \leqslant 0{\cdot}35$. Data taken using stationary hot-wire located 1·5 mm downstream of blade trailing edge. P and S are the high and low pressure sides of the blades, respectively.

4.3. ROTATING SENSOR MEASUREMENTS

Additional velocity measurements were performed at locations within a blade passage using a rotating hot-wire sensor, again oriented to maximize sensitivity in the axial and tangential directions. The sensor was connected to the data acquisition hardware via a multi-channel slip ring located at the end of the motor shaft. Since the sensor was rotating with the impeller, synchronous averaging of the data was not necessary. The average values for each measurement location were calculated from entire data blocks which were 160k samples long (i.e. $n = 160\,000$). For the representative data to be discussed, the fan was rotating at a speed of 2040 rpm and $\phi \approx 0{\cdot}3$. The induced electrical noise levels were monitored to ensure that the signal-to-noise levels were not adversely affecting the data.

Figures 11 and 12 contain the mean velocity and turbulence intensity data for sensor positions located at the mid-span of the blade (i.e. measurement locations which lie on a cylinder whose radius was $r_m = 3{\cdot}6$ cm, as shown in Figure 2). Figure 10 is an orientation diagram for Figures 11 and 12. The abscissa (x) is the distance to the measurement point from the leading edge of blade #1 (the leading blade). This is expressed as a percentage distance by dividing by the total distance from the LE to the TE. The ordinate (y) is the distance along the arc connecting the suction side of the blade #1 (see Figure 10) to the pressure side of blade #2 (the trailing blade). This is expressed as a percentage distance by dividing by the total arc distance between blades. Both distances are specified as percentage distances because of the complexity of the passage geometry. For example, at a constant radius, the total distance between blades varies with x. The contour data shown in the figures was interpolated from 48 sensor positions. A full scan over the entire range of y is not presented here because some locations next to blade

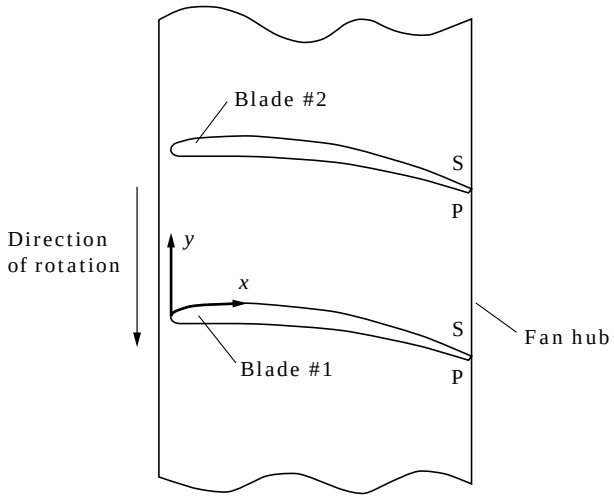

Figure 10. Orientation diagram for measurements made in impeller passage. The observer is out beyond the blade tips looking down into the blade channel, toward the impeller hub. P and S are the high and low pressure sides of the blades, respectively. (This figure is not drawn to scale and is not intended to fully depict blade geometry.)

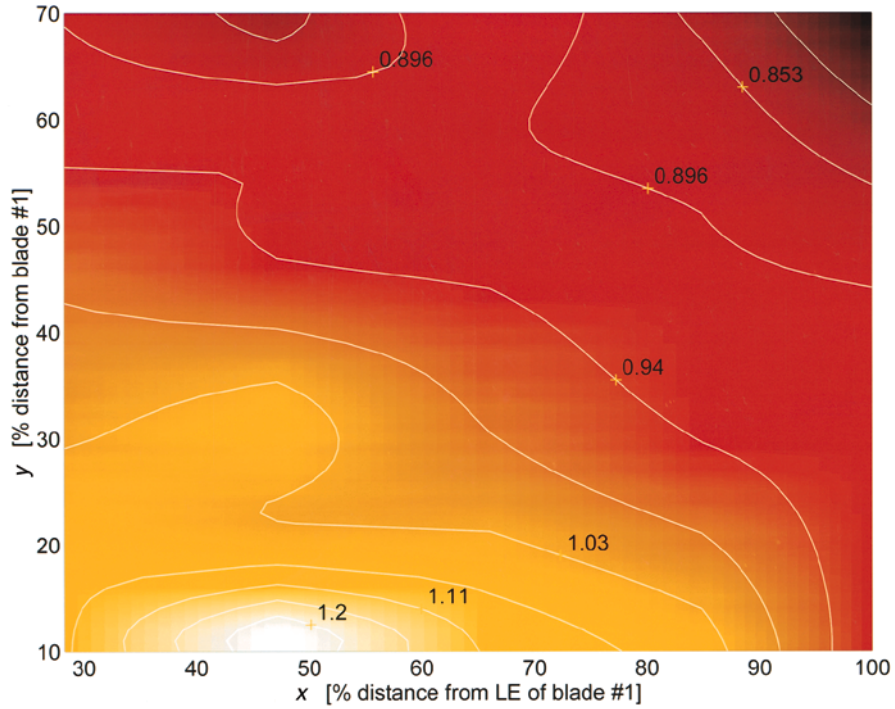

Figure 11. Passage mean velocity contour plot for mid-span sensor locations and with $\phi = 0{\cdot}3$. Data taken using sub-miniature straight hot-wire sensors placed at 48 measurement passage locations.

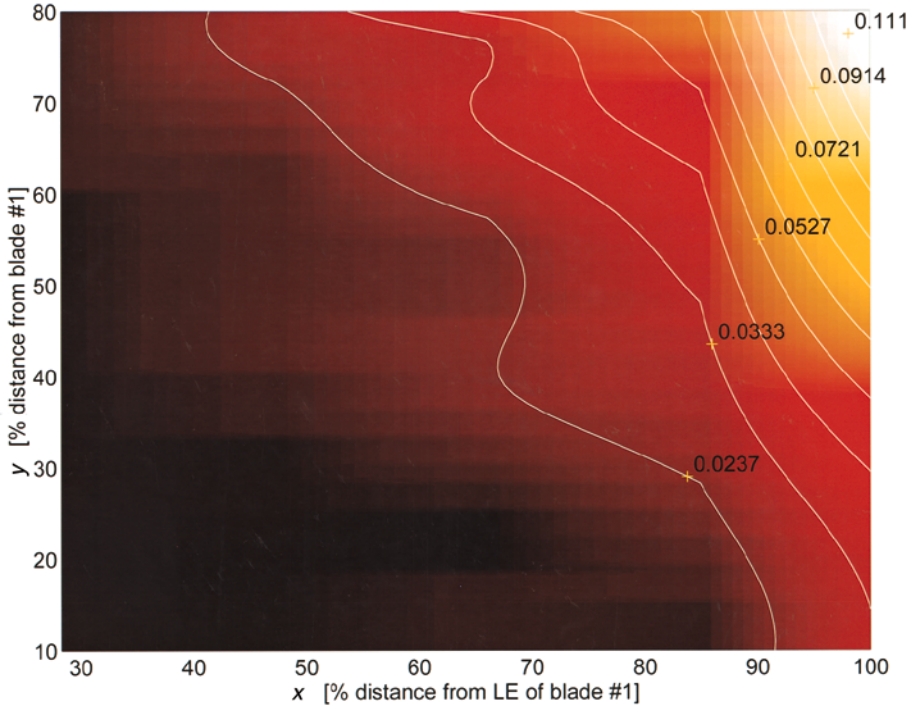

Figure 12. Passage turbulence intensity contour plot for mid-span sensor locations and with $\phi = 0{\cdot}3$. Data taken using sub-miniature straight hot-wire sensors placed at 48 measurement passage locations.

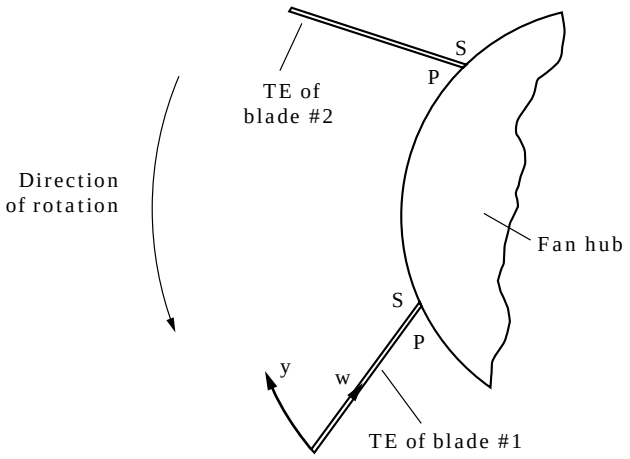

Figure 13. Orientation diagram for measurements made across impeller exit plane. The observer is downstream of the blade trailing edges looking upstream into the blade channel. P and S are the high and low pressure sides of the blades, respectively. (This figure is not drawn to scale and is not intended to fully depict blade geometry.)

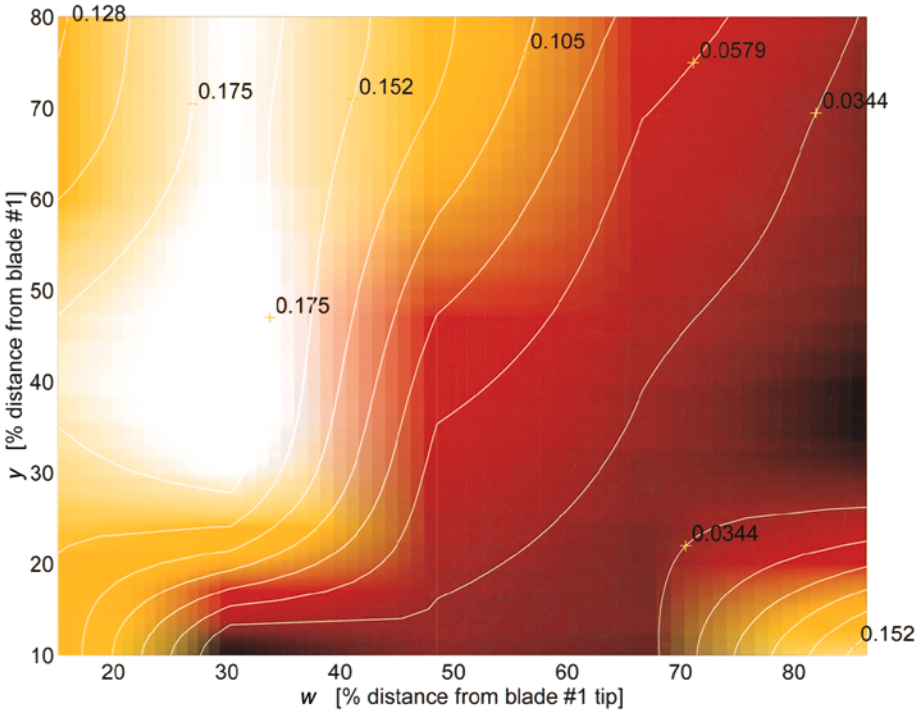

Figure 14. Passage turbulence intensity contour plot across impeller exit plane and with $\phi = 0{\cdot}3$. Data taken using sub-miniature straight hot-wire sensors placed at 48 measurement passage locations.

surfaces were not accessible. The lack of a complete data set, coupled with the fact that there are sharp transitions in the turbulence intensity near some blade surfaces, caused large errors when an interpolation over all y was attempted. As a result, the dimensions of the scan were limited as noted.

As shown in Figure 11, the mean velocity data had its maximum approximately 20 mm from the blade's leading edge, on the suction side of blade #1. This location corresponds to the point at which the blade has its maximum thickness and lift. In Figure 12, the turbulence intensity rises to a maximum of approximately 0·11 near the TE of blade #2. This result corresponds to both the flow visualization observations and the earlier outlet stationary sensor data which indicated that a substantial region of the flowfield was turbulent near the fan exit (i.e. close to the TE of the blades), particularly on the pressure side of the blades.

Scans taken over the surface located near the tip and hub demonstrated the same trend toward an increase in the turbulence intensity near the TE on the pressure side of blades. (There were again indications in the tip scan data that the middle of the passage was turbulent. It was unclear whether or not this was due to tip vortex flow, or to the build-up of a boundary layer near the tube wall, as suggested earlier.)

A similar set of measurements was taken over a planar surface located near the exit of the passage (approximately 53 mm from the leading edge of the blades, as measured along the blade surface). As shown in Figure 13, the abscissa for this measurement (w) is the percentage distance from the tip to the root of the blade and the ordinate (y) is again the percentage arc distance from the suction side of blade #1 to the pressure side of blade #2. The measurement surface was perpendicular to the axial direction (see Figure 2). For this scan, $10 \geqslant y \geqslant 80$, and the data was again interpolated from 48 measurement positions.

As can be seen in Figure 14, the turbulence intensity was highest in the region between the blade mid-span and the blade tip. Once again, the values were highest toward the TE of blade #2. There is also a small region of high turbulence intensity in the lower right hand corner of the figure. The likely cause of this was a "corner" vortex flow. Such flows tend to form at locations where perpendicular surfaces meet. In this case, a vortex probably formed at the location where the blade meets the fan hub.

The final set of rotating hot-wire data presented here is from a series of 12 measurement locations lying along the pressure side of blade #2. All locations were 5 mm from the blade tip and 1–2 mm out from the blade surface (see Figure 15). The turbulence intensity data for this data set is shown in Figure 16. The initial rise over the first 10 mm of the blade was possibly due to the build-up of the surface boundary layer or some degree of leading edge separation. The turbulence intensity then dropped off somewhat before beginning to increase again at a distance of approximately 20 mm. As noted earlier, this location on the blade corresponded to the tip area where the blade lift would be highest and was also the region of the blade where the tip vortex began to form. The large pressure differential across the gap at this location gave rise to a strong tip gap flow which, in turn, resulted in the formation of the vortex on the suction side of the blade. The rise in turbulence intensity may have been due to the increased tip gap flow.

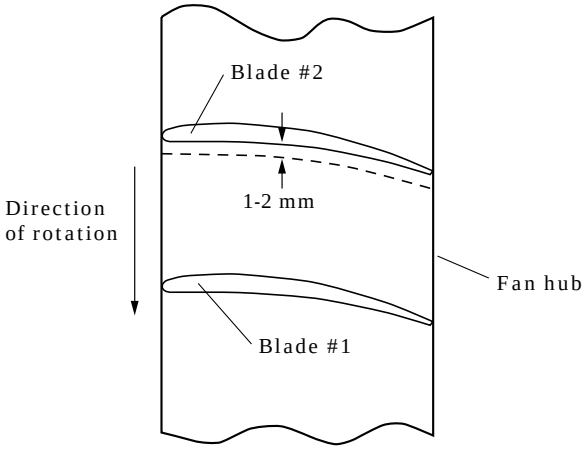

Figure 15. Orientation diagram for measurements made along blade tip. The observer is out beyond the blade tips looking down the blade channel and toward the impeller hub. (This figure is not drawn to scale and is not intended to fully depict blade geometry.)

At locations farther from the LE, the turbulence was presumably due to a mixture of the tip gap flow of the blade that the sensor was near, and the tip gap flow from the previous blade.

The fluid dynamic measurements described in this section were not repeated using the plenum facility. While this would have been an interesting avenue to pursue, a considerable amount of time would have been required to redesign and

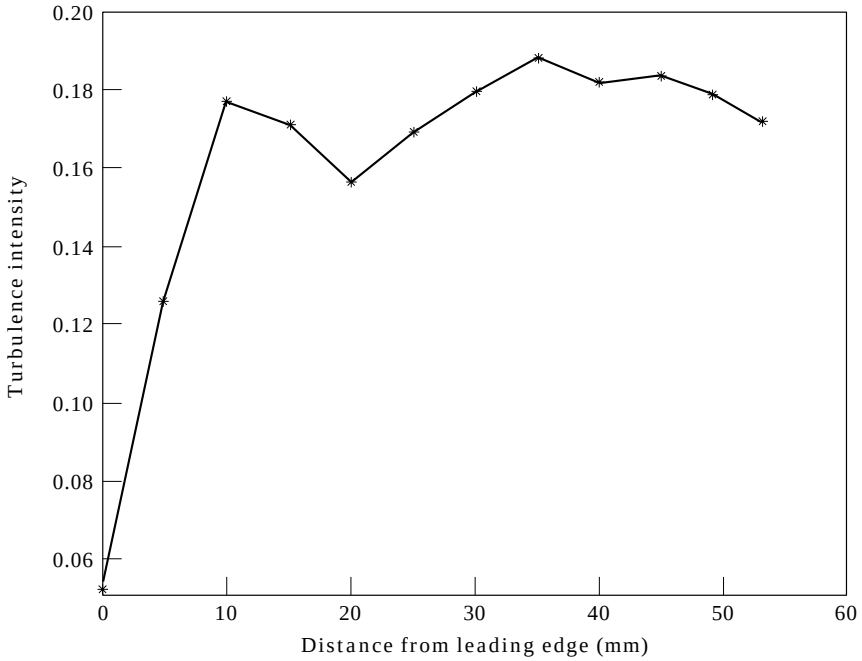

Figure 16. Turbulence intensity measured near blade tip on the pressure side and with $\phi = 0{\cdot}3$. Sub-miniature straight hot-wire located 1–2 mm from blade surface.

instrument the facility for such measurements, and it was not clear that such measurements were necessary. Given that the wind tunnel data discussed above (as well as, the wind tunnel and plenum flow visualization work) indicated that flow unsteadiness related to tip vortices might be an important source of noise for the test fan, the focus of the study became an investigation to determine if such a conclusion was warranted. As will be described, the ANSI test plenum was used exclusively for the acoustics work since it was designed to provide operating conditions which are close to those seen by a fan in an actual application. This approach did not seem unreasonable given that the performance region of interest was $0{\cdot}25 < \phi < 0{\cdot}35$ and, as noted earlier, the performance curves were similar in this region for both test facilities.

5. RADIATION OF BROADBAND NOISE

As the discussion in the previous sections demonstrates, observations from flow visualization experiments and data from hot-wire sensor measurements indicated that tip vortices were primary contributors to turbulence within the blade passages of the test fan, particularly near the impeller exit and close to the pressure sides of the blades. There were further indications that other turbulent regions were located near some blade surfaces and the casing wall. In general, any or all of these turbulent regions could be aeroacoustic sources of broadband noise.

Experimental determination of the contribution of each turbulent region to the radiated noise would be expected to be difficult. These source regions represent a distributed set of noise sources. The source distribution within each blade channel is incoherent with respect to the source distributions in all other blade passages since the tip vortices and boundary layers within each passage are independently formed. Similarly, regions within each blade passage will be incoherent with respect to each other, depending upon the turbulent eddy size. Consequently, the coherence between hot-wire (and/or surface hot-film) sensors and farfield microphones would be expected to be low. An upper bound on such a measurement can be obtained by assuming that the dominant radiation is associated with relatively large scale eddies caused by the five independent tip vortices. Under such circumstances, coherence values between a sensor located in the blade passage and a far-field microphone could reach 0·2 assuming ideal conditions. However, since most of the associated broadband radiation will be attributable to a distribution of much smaller eddies, coherence measurements are unlikely to add insight into the generation of broadband noise. No attempt was made here to obtain detailed information regarding the spatial extent and length scale distribution of the turbulence. Despite the lack of this information, the discussion above can be combined with other investigators' results to provide speculation as to how these regions of turbulence result in the generation of broadband acoustic energy.

5.1. SOURCE FREQUENCY REGIMES

As implied above, a key issue to consider in the radiation of broadband noise from an air-moving device is the extent to which the aeroacoustic sources are

acoustically compact. For the impeller, the transition from compact to non-compact radiation will occur when the tips of all of the impeller blades are no longer located within an acoustic wavelength (i.e. $D/\lambda < 1$). At frequencies above an impeller transition frequency (f_{imp}), the acoustic noise is presumed to be generated by a set of independent aeroacoustic sources distributed throughout the impeller. These sources will be created by the time-varying non-linear self-interaction of turbulent eddies in the flow, and by the interaction of the eddies with the impeller. The location, strength and relative phase of these sources are the key time-varying quantities. Below the impeller transition frequency, large scale disturbances such as net unsteady impeller lift-related reaction forces would be the likely cause of broadband noise. For such sources, source strength is the primary variable.

For the blades, the transition from compact to non-compact radiation will occur when the blade leading and trailing edges are no longer located within an acoustic wavelength (i.e. $C/\lambda < 1$). At frequencies above a blade transition frequency (f_{bl}) the acoustic noise is generated by a set of independent aeroacoustic sources distributed across the blade surface. The relative size of the sources is determined by the correlation lengths of the eddies. Below f_{bl} the entire blade can be treated as a single source.

As the frequency rises from f_{imp} to f_{bl}, the blade-to-blade source relationship changes. As noted above, below f_{imp} the blade-to-blade phase variation may be very small. Within the regime between f_{imp} and f_{bl}, the individual blades will begin to act as independent sources.

The impeller and blade transition frequencies can be estimated using

$$f_{imp} \approx a/D, \qquad f_{bl} \approx a/C, \tag{6, 7}$$

where D is the diameter of the impeller, a is the speed of sound, and C is the chord length of the blades. For the fan studied here, the impeller and blade transition frequencies are 2·4 and 6·6 kHz, respectively. It is important to note that these transition frequencies are based on fixed dimensions and therefore do not scale with fan speed (or Strouhal number).

Excluding turbulence that may be ingested by the fan, the key turbulent regions of the measured flowfield appear to be associated with tip vortex flows. This tip gap flow gives rise to a distribution of turbulent eddies within the blade passages. Since the largest eddy dimension is bounded by the vortex core size, and the vortex core will be small compared to the impeller dimensions, the associated radiation can be characterized as non-compact. However, the dimensions of the largest turbulent eddies may be of the same order of magnitude as the blade chord length. As such, it is likely that the frequency regime of the radiation associated with these turbulent eddies will begin at or above f_{imp}.

In aeroacoustic studies of both fixed and rotating lifting surfaces, it has been shown that one source of high frequency noise can be associated with the interaction of turbulence with the trailing edge of the lifting surface. As turbulence passes over the trailing edge of a blade, a set of distributed sources lying along the blade edge is created. The size, strength and phase of each of these local sources is controlled by several characteristics of the turbulent eddies: the

spanwise location, size, strength, and convection speed of the independent eddies (quantified using correlation length measures). These characteristics will determine the frequency regime and magnitude of the radiation. (A detailed discussion, as well as a thorough set of references, can be found in reference [15].) In most experimental studies of trailing edge noise, the turbulence is caused by either separation of the flow as it passes over the suction side of the blade, or it is associated with the growth of the surface boundary layer. As the earlier discussions show, a key source of edge turbulence in the fan tested here is caused by tip gap flows. While the source of the turbulence is different, the associated trailing edge scattering mechanism would presumably be the same.

Assuming that trailing edge noise is indeed a dominant source, Blake's empirical analysis of trailing edge noise can be used to provide an estimate of the frequency regime of the associated acoustic emission [15]. A rough estimate of the lower frequency bound for trailing edge noise, f_{te}, is obtained using

$$f_{te} \approx 0{\cdot}1 V_{tip}/h_m, \tag{8}$$

where h_m is the maximum thickness of the blade (approx. 4·5 mm). The fact that f_{te} is directly proportional to tip speed and inversely proportional to eddy size (h_m is used as an indicator of expected eddy size) can be explained in physical terms. The convection velocity of eddies as they pass the trailing edge is directly proportional to V_{tip}. When large eddies are travelling slowly, the time scale of the disturbance at the TE is relatively long and the frequency of the resulting acoustic radiation is low. Conversely, when small eddies are travelling quickly, the time scale of the disturbance at the TE will be relatively short and the frequency of the resulting acoustic radiation will be high.

The relevant tip speed range for this fan is $13{\cdot}4 \geqslant V_{tip} \geqslant 26{\cdot}8$. This yields a range for the lower frequency bound of approximately

$$300 \geqslant f_{te} \geqslant 600. \tag{9}$$

Section 6 presents sound pressure level data for a series of experiments where the fan tip speed was 24·5 m/s. The corresponding value for f_{te} is 545 Hz.

The results discussed so far have not presented any insight into the likely sources of low-frequency noise. Using data from Wright and others, Blake argues that noise related to the ingestion of turbulence and/or blade loading is likely to dominate the spectra of axial-flow devices at low frequencies [15]. Again based upon empirical results, the centre frequency for the band over which loading/ingestion noise is likely to dominate the spectrum can be estimated using

$$\frac{0{\cdot}6 V_{tip}}{C} \geqslant f_{li} \geqslant \frac{1{\cdot}1 V_{tip}}{C}. \tag{10}$$

The 20 dB down points are estimated to be located at

$$f_{low} = 0{\cdot}125 f_{li}, \qquad f_{high} = 8 f_{li}. \tag{11, 12}$$

Based again upon a representative tip speed of 24·5 m/s the above equations yield a mean f_{li} of 400 Hz and a mean bandwidth of 50–3200 Hz. Coupled with the

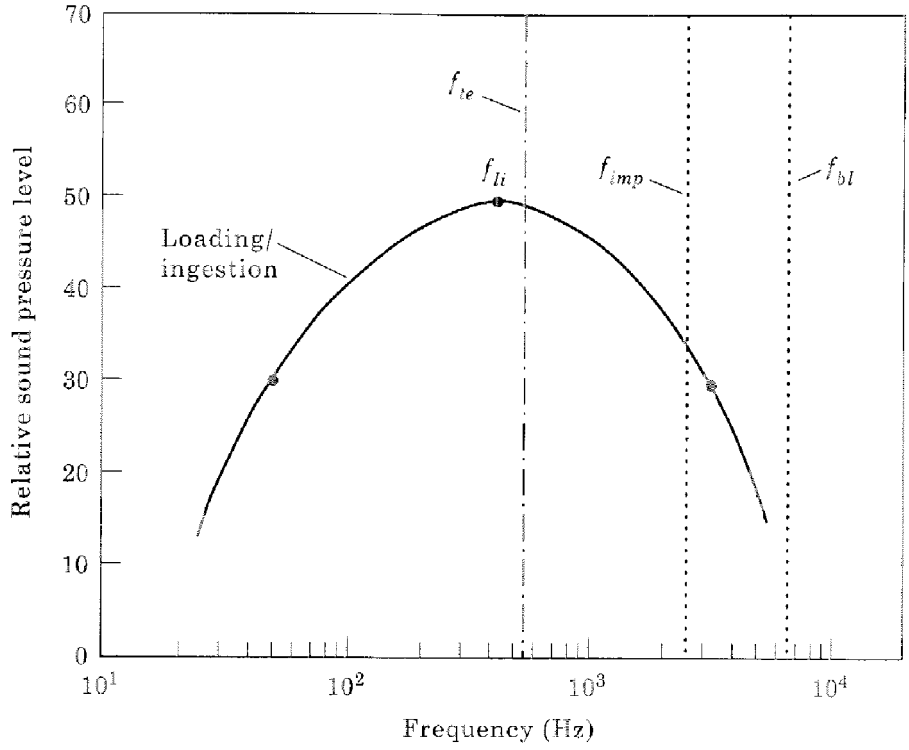

Figure 17. Empirical estimates for loading/ingestion noise frequency band and for primary dimensional transition frequencies.

earlier estimates for f_{tr} and f_{te}, Figure 17 presents an overview of the estimated frequency regimes for some of the aeroacoustic mechanisms of interest here. Generally, the loading/ingestion noise would be expected to dominate the acoustic spectrum below approximately 500 Hz. Similarly, the influence of the turbulent regions described earlier would be expected to begin influencing the spectrum within the range of 500–2500 Hz. Above this transition region, these turbulent sources should dominate the spectrum.

It should be noted that the Reynolds number (based on chord) for the data used by Blake is an order of magnitude higher than for the test fan used here. Consequently, the applicability of his conclusions is somewhat unclear.

6. ACOUSTIC MEASUREMENTS

The above sections presented data indicating that tip gap flows were a primary source of small-scale turbulence in the impeller flowfield. Based upon observations of the turbulence and empirical estimates of relevant frequency regimes, this turbulence was identified as a likely source of high frequency noise. The suggested radiation mechanisms were trailing edge scattering and radiation from free turbulence. An additional possible noise source was the turbulence present in the blade passages, the casing or blade boundary layers, and in the flow downstream of the fan. Since radiation from turbulence is an inherently less efficient mechanism than trailing edge scattering (quadrupole vs edge dipole), the influence of such sources can be hard to discern.

Assuming that these turbulent regions are indeed sources of broadband noise, a set of approaches for noise reduction becomes apparent. By applying design modifications and evaluating the extent to which they are successful, the significance of the proposed noise sources can be ascertained. This section discusses experiments that address the question in this way.

The ANSI S12.11 test plenum described in section 2 was used in a series of fan modification experiments. As noted earlier, the plenum was designed to provide flow conditions which would be similar to normal installation conditions for this type of fan. In contrast, the inlet boundary layer and the general inlet/outlet airflow conditions in the wind tunnel would not be expected to be representative of typical operating conditions. Therefore, all of the acoustic measurements described here were made using the plenum. An important detail to note is that the plenum inflow conditions were not changed during the tests. Thus, inlet boundary layer conditions could be largely eliminated as a variable. (If a future study focuses on low frequency noise sources where the ingestion of large scale turbulence would be a possible source of noise, separate fluid dynamic measurements made using the plenum facility would probably be an essential part of the work.)

As part of the acoustic tests, both narrowband sound pressure and octave band sound power measurements were made. Sound pressure spectra were measured 1 meter from the fan inlet at on-axis, 30° off-axis and 60° off-axis positions. The data was taken using Brüel & Kjær 4134 $\frac{1}{2}''$ microphones, and measurements were made at four non-dimensional fan operating points: $\phi = 0{\cdot}25$, $0{\cdot}29$, $0{\cdot}32$, $0{\cdot}35$. The on-axis position sound pressure data for $\phi = 0{\cdot}32$ is presented here since that data is representative of the results obtained. Sound power measurements were also made in order to provide an indication of the global noise reduction attributable to the design changes. The sound power measurements were made in a $10{\cdot}4 \times 8{\cdot}2 \times 8{\cdot}5$ m anechoic test chamber using the method described in ANSI S12.11 [9].

During the tests, measurements of aerodynamic performance were performed before and after modifications to the fan were made. While the overall shape of the performance curves remained consistent, the performance of the fan was slightly degraded (1–5%) after some modifications. In order to compensate for this, the acoustic measurements were always performed with the test fan running at the fixed system operating points noted above (i.e. at fixed plenum pressure drop and flow rates). In practice, the fan speed was raised as needed to compensate for loss of performance. The end result was that the aerodynamic load conditions and fan operating point were equivalent for each comparison, and the measured acoustic changes were therefore indicative of those that would be seen when applied in an actual system cooling design.

The first two noise reduction experiments focused on methods for modifying the characteristics of the tip gap flow. The goal was to reduce the energy in the tip vortex by inhibiting flow through the gap. The most obvious method for achieving this result was to reduce the tip gap dimension. Starting with a standard Papst 6248 fan, measurements were made with 3 different tip gap dimensions. The noise reduction increased as the tip gap was reduced, and there was no significant

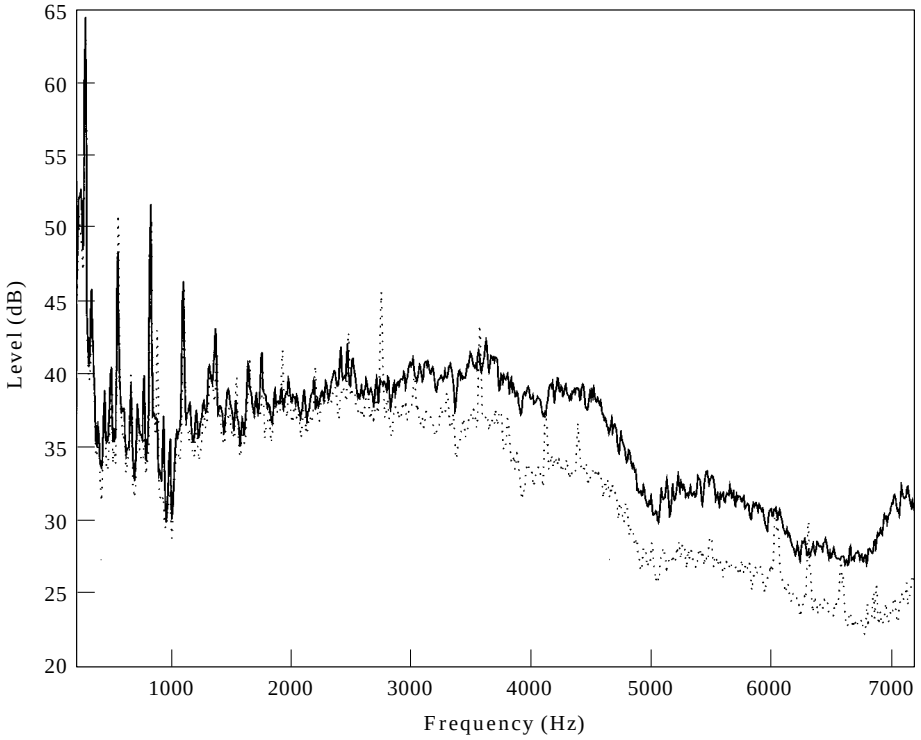

Figure 18. Typical broadband acoustic spectra corresponding to standard tip gap of 6·3 mm (——) and to reduced tip gap of 2·3 mm (· · · ·). Operating point set to $\phi = 0{\cdot}32$.

difference in noise reduction across the five operating points. The typical effect of this modification is shown in Figure 18 which compares sound pressure data before and after changing the tip gap from 6·3 mm (roughly the production tip gap value) to 2·3 mm (the smallest tip gap tested). As shown in Table 2, the decrease in the tip gap resulted in a broadband sound power reduction of 1–8 dB from 2 to 8 kHz. The noise reduction occurred at high frequencies with an onset frequency that compared favorably with the transition frequency estimates discussed in section 5. The velocity dependence study mentioned earlier provided further evidence supporting the premise that a significant source transition occurred near 2 kHz [8].

As discussed in reference [13], reducing the tip gap to this extent is a poor solution for these types of fans. The required manufacturing and operating

TABLE 2

Measured sound power reductions due to test fan modifications (dB)

	250 Hz	500 Hz	1 kHz	2 kHz	4 kHz	8 kHz
Reduced tip gap	0	−2	−1	1	3	8
Flanges added	0	−2	−1	1	5	5
TE fabric added	2	0	1	4	3	2
Flanges and fabric	1	−2	0	4	9	9

condition tolerances cannot be held without an unacceptable increase in the per unit cost of the fans. Also, as the data in Figure 18 demonstrates, small tip gaps can result in an increase in the level and number of blade passage tones. The increase in tone levels occurs because, at reduced tip gap values, irregularities in the casing or a slight shaft eccentricity results in a larger percentage variation in the circumferential tip gap.

Since the tip gap flow is driven by the pressure difference between the suction and pressure sides of the blades, an alternative method for reducing the tip gap flow is to add flanges to the blade tips, as shown in Figure 19. If the flanges are wide enough in the circumferential direction, the pressure differential across the gap is reduced, decreasing the flow through the gap. Six flange designs were tested and the on-axis sound pressure results obtained using the best design are shown in Figure 20. In this design, the maximum distance from the blade surface to the flange edge was approximately 6 mm. Similar to the reduced tip gap data, the noise reduction primarily occurred above 2 kHz with a maximum sound power reduction of 5 dB. For these tests, the blade tips were shaved before the flanges were attached so that the tip gap dimension was always 6·3 mm. (Another method for reducing tip gap flow involves the use of a rotating shroud [12]. This approach was not thoroughly pursued as part of this study since the tip gap reduction and tip flange tests adequately demonstrated that modifying the tip gap flow lowers levels at high frequencies.)

The addition of the flanges to the blade tips may have also altered the aeroacoustic interaction of the blade tips with the ingested boundary layer. To this point, such an effect was assumed to have been relatively weak. The data from the shroud experiments mentioned above implied that effects attributable to the ingested boundary layer are not significant in this high frequency regime [11]. However, while the flow reduction explanation noted above is physically compelling, further measurements would be needed to definitively eliminate inlet boundary layer effects as a contributing source of high frequency noise.

Based upon the assumption that trailing edge scattering might be a significant aeroacoustic mechanism, blade trailing edge modifications were also tested as a potential method for reducing high frequency noise. The relevant scattering theory indicates that the radiation generated at the trailing edge is dependent upon several physical properties of the edge. In particular, the geometry, compliance and acoustic impedance of the edge are key parameters. While the theory cannot yet be used to specify the optimal values for these parameters, experiments with various materials demonstrated positive results.

Representative sound pressure data from the most effective method is presented in Figure 21. In this experiment, a strip of Velcro loop material (approximately 3 mm wide) was attached to the trailing edges of the fan blades (see Figure 19). The material was attached to the pressure side of the blades, and was run across the span of the blade. As the sound power data demonstrates, this modification provided 1–4 dB of noise reduction above 500 Hz. Generally, the results again compared favorably with the estimated transition frequencies shown in Figure 17. The data from the four operating point tests consistently showed that this trailing

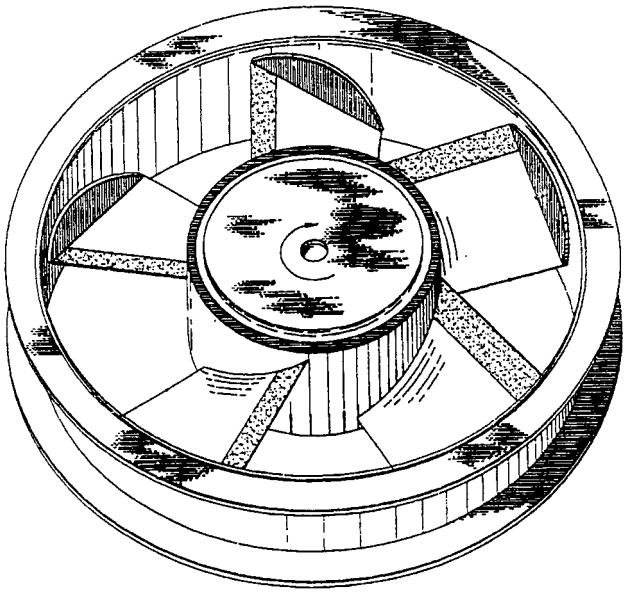

Figure 19. Sketch of a fan with tip flanges and modified trailing edges. (Not drawn to scale.)

edge modification was most effective between 2 and 4 kHz. The implication of that observation was that the trailing edge scattered components were most significant in the 2–4 kHz region. This conclusion is further supported by the experiments discussed in reference [8].

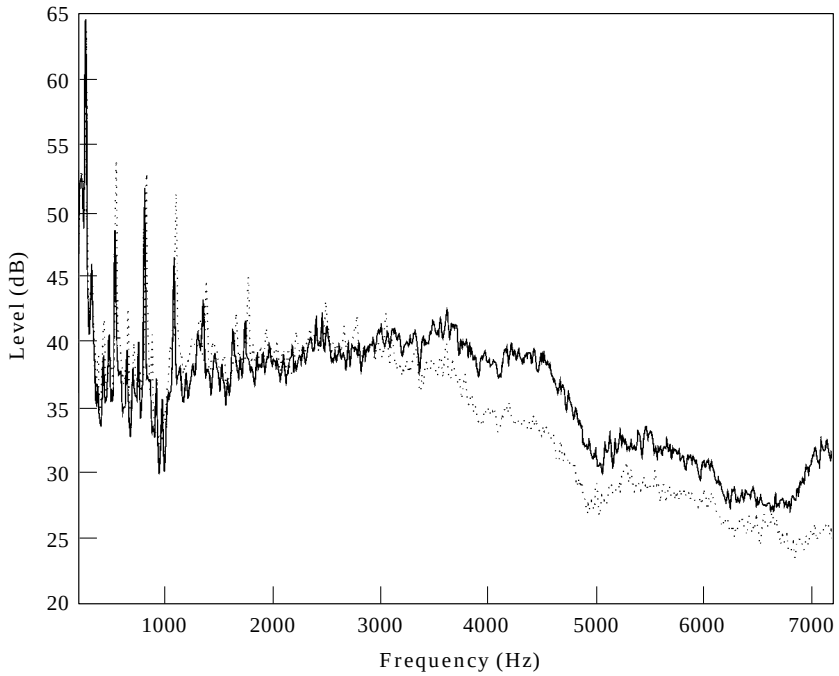

Figure 20. Typical broadband acoustic spectra corresponding to impeller with (· · · ·) and without (——) tip flanges. Operating point set to $\phi = 0{\cdot}32$.

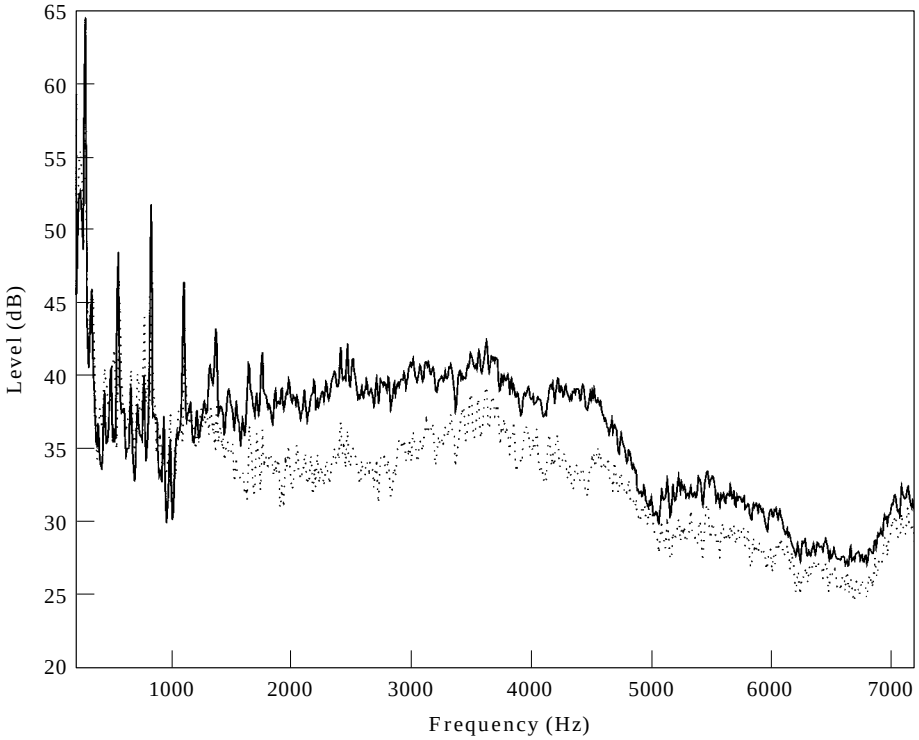

Figure 21. Typical broadband acoustic spectra corresponding to impeller with (· · · ·) and without (——) fabric attached to trailing edges. Operating point set to $\phi = 0{\cdot}32$.

For completeness, further measurements were made with material attached to other blade locations including the trailing edge on the suction side of the blades, the middle section on the pressure side of the blades, etc. These modifications provided no improvement and, in several instances, increased the level of noise generated and significantly degraded fan performance. In several cases, the cause for the degradation was obvious. For example, as noted earlier, the measured turbulence intensity values were low on the suction sides of the blades indicating the turbulence convected over the trailing edge on the suction side was relatively low. As such, adding material to the suction side of the blades did not provide an acoustic benefit, and degraded the fan performance presumably due to adverse affects on the unseparated flow that otherwise existed over the surface.

When the trailing edge fabric was used in conjunction with the tip flanges, the noise reduction obtained was 0–9 dB above 1 kHz, as shown in Figure 22 and Table 2. The data demonstrated that the combination of the two methods provided a significant reduction in the amount of high frequency noise generated. Presumably, the total amount of noise reduction was not equal to the sum of the noise reductions achieved for each individual modification because the proposed effects of the modifications were not independent. That is, the unsteadiness attributable to the tip vortices was the fluid dynamic source of energy in both cases.

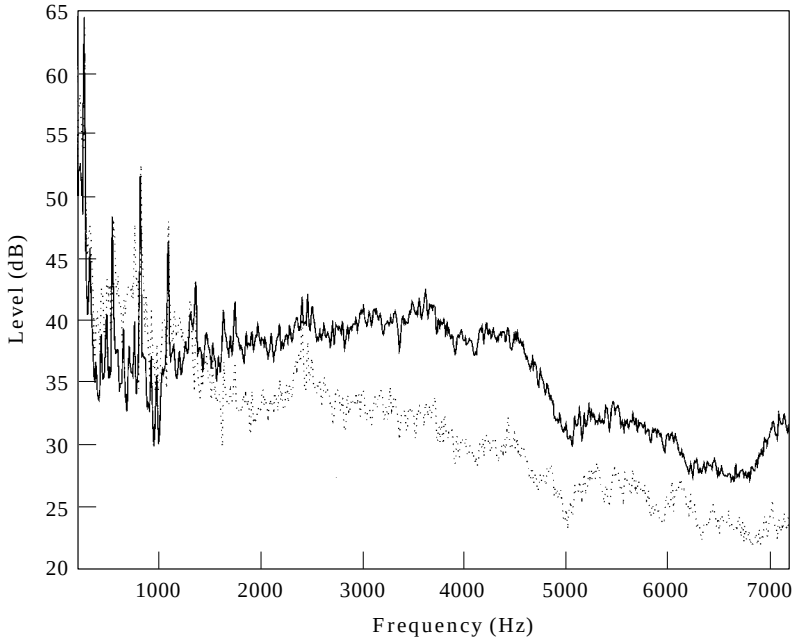

Figure 22. Typical broadband acoustic spectra corresponding to impeller with (· · · ·) and without (——) both tip and trailing edge modifications. Operating point set to $\phi = 0{\cdot}32$.

The acoustic results discussed in this section provide support for the premise that flow unsteadiness related to the tip gap vortex was a primary source of high frequency noise. Furthermore, the data also supported the position that a primary aeroacoustic mechanism in the conversion of turbulence energy into broadband noise was trailing edge scattering. A secondary mechanism for the fan may have been radiation from free turbulence in the flowfield, and/or radiation from casing or blade boundary layers.

Similarly, the acoustic data reinforced the premise that there was a low frequency regime controlled by other aeroacoustic sources. These sources were likely to be associated with acoustically compact generation mechanisms. More specifically, given the estimates shown in Figure 17, the dominant source(s) may have a spatial extent comparable to the blade dimensions or, possibly, comparable to the entire impeller. A likely candidate is noise generation attributable to variations in blade loading [3, 4, 15].

7. CONCLUSION

Fluid dynamic and acoustic data presented in this paper indicated that tip gap flows are significant contributors to the broadband noise generated by small axial flow fans. Acenephthene coated impellers and smoke flow visualization tests provided subjective evidence that flow unsteadiness in the impeller channels was caused by tip gap flows. Stationary hot-wires placed downstream of the impeller and rotating hot-wires placed within blade channels provided a quantitative description of the non-radial components of that unsteadiness. Using the results

from the flow visualization and hot-wire tests, possible noise generation mechanisms were postulated. Impeller modifications were then made to test the viability of the proposed noise contributors. The addition of flanges to the blade tips and of fabric near the blade trailing edges provided as much as 9 dB of noise reduction above 1 kHz.

Taken as a whole, the experimental evidence strongly indicated that unsteadiness attributable to tip gaps flows was a dominant source of noise above 1 kHz. The data also provided circumstantial evidence that the relevant aeroacoustic mechanisms were trailing edge scattering and radiation from free turbulence and/or boundary layer radiation. Based upon source transition frequency estimates, the onset of the measured noise reduction at 1 kHz lent support to the physical explanation. Further study will be needed before it can be absolutely stated that these mechanisms have been correctly identified.

While the results presented here may be broadly applicable to the small axial fans used in electronic system cooling, and similar impeller modifications may provide benefit when applied to other types of air-moving devices, the study does not address an essential problem. In order to significantly reduce the perceived noise generated by small axial fans, it is clear that the results presented here will need to be coupled to an analogous study of low frequency noise generation. Since a typical small axial fan spectrum contains both significant broadband energy and prominent tones below 1 kHz, the reduction of high frequency noise alone will not provide the desired reduction in perceived loudness or annoyance.

ACKNOWLEDGMENTS

The authors would like to acknowledge the contributions of L. Mongeau and G. C. Lauchle who were key contributors in the initial stages of this study. M. H. Krane provided valuable comments on early versions of this paper. The authors also owe great thanks to R. Kubli who turned roughly drawn sketches into superb test facilities.

REFERENCES

1. D. A. Quinlan 1997 *Proceedings of Noise-Con* 97 (C. B. Burroughs, ed.), 65–70. Future trends in acoustic noise emission for telecommunications and information technology equipment.
2. W. R. Kundert 1985 *Proceedings of Noise-Con* 85 (G. C. Maling, ed.), 127–132. Fan speed control for noise control.
3. W. Chiu, G. C. Lauchle and D. E. Thompson 1989 *Journal of the Acoustical Society of America* **85**, 641–647. Subsonic axial flow noise and unsteady rotor force.
4. G. Maling 1994 *Noise Control Engineering Journal* **42**(5), 159–169. Historical developments in the control of noise generated by small air-moving devices.
5. W. Neise and G. H. Koopman 1988 *Proceedings of Inter-Noise* 88 (M. Bockhoff, ed.), 801–804. Active source cancellation of the blade tone fundamental and harmonics in centrifugal fans.
6. D. A. Quinlan 1992 *Noise Control Engineering Journal* **39**(3), 95–101. Active control of tones radiated from small axial flow fans.

7. G. C. Lauchle, J. R. MacGillivray and D. C. Swanson 1997 *Journal of the Acoustical Society of America* **101**(1), 341–349. Active control of axial-flow fan noise.
8. D. A. Quinlan 1997 *Journal of the Acoustical Society of America*. Frequency dependent velocity scaling of aeroacoustic source spectra. In press.
9. ANSI S12.11 American National Standard: method for the measurement of noise emitted by small air-moving devices.
10. L. R. Taylor 1994 *Proceedings of Noise-Con* 94, 53–58. Acoustical and fluid dynamic similarity for air-moving device measurements on the ANSI test plenum.
11. R. E. Longhouse 1976 *Journal of Sound and Vibration* **53**(1), 25–46. Vortex shedding noise of low tip speed, axial flow fans.
12. R. E. Longhouse 1978 *Journal of Sound and Vibration* **58**(2), 201–214. Control of tip-vortex noise of axial flow fans by rotating shrouds.
13. T. Fukano, Y. Takamatsu and Y. Kodama 1986 *Journal of Sound and Vibration* **105**(2), 291–308. The effects of tip clearance on the noise of low pressure axial and mixed flow fans.
14. F. Chamber, T. Nawrot and W. Neise 1992 *Proceedings of the DGLR/AIAA Aeroacoustics Conference*. AIAA paper no. 92-02-40, 250–259. Experimental investigation of tip clearance noise in axial flow machines.
15. W. K. Blake 1986 *Mechanics of Flow-Induced Sound and Vibration*. New York: Academic Press.